Ultrasonics 108 (2020) 106171

Contents lists available at ScienceDirect

Ultrasonics

journal homepage: www.elsevier.com/locate/ultras

Determining the crystallographic orientation of hexagonal crystal structure materials with surface acoustic wave velocity measurements

Paul Dryburgh[a], Richard J. Smith[a], Paul Marrow[a], Steven J. Lain'e[b], Steve D. Sharples[a], Matt Clark[a], Wenqi Li[a,*]

[a] Optics and Photonics Group, Faculty of Engineering, University Park, University of Nottingham, NG7 2RD, UK
[b] Department of Materials Science and Metallurgy, University of Cambridge, 27 Charles Babbage Road, CB3 0FS, UK

ARTICLE INFO

Keywords:
Orientation determination
Crystallographic characterisation
Surface acoustic waves
Hexagonal crystal
Grain structure

ABSTRACT

Throughout our engineered environment, many materials exhibit a crystalline lattice structure. The orientation of such lattices is crucial in determining functional properties of these structures, including elasticity and magnetism. Hence, tools for determining orientation are highly sought after. Surface acoustic wave velocities in multiple directions can not only highlight the microstructure contrast, but also determine the crystallographic orientation by comparison to a pre-calculated velocity model. This approach has been widely used for the recovery of orientation in cubic materials, with accurate results. However, there is a demand to probe the microstructure in anisotropic crystals - such as hexagonal close packed titanium. Uniquely, hexagonal structure materials exhibit transverse isotropic linear elasticity. In this work, both experimental and simulation results are used to study the discrete effects of both experimental parameters and varying lattice anisotropy across the orientation space, on orientation determination accuracy. Results summarise the theoretical and practical limits of hexagonal orientation determination by linear SAW measurements. Experimental results from a polycrystalline titanium specimen, obtained by electron back scatter diffraction and spatially resolved acoustic spectroscopy show good agreement (errors of $\phi_1 = 5.14°$ and $\Phi = 6.99°$). Experimental errors are in accordance with those suggested by simulation, according to the experimental parameters. Further experimental results demonstrate dramatically improved orientation results (Φ error $<1°$). Demonstrating the possibility of achieving results near the theoretical limit by strict control of the experimental parameters.

1. Introduction

Most functional materials used in high-value engineering form into crystalline states whereby the orientation of these lattices contribute significantly to the functional properties. Anisotropic lattice properties include: elasticity and magnetism [1], and have profound effects on the fatigue [2] and creep resistance [3]. It is therefore especially important to measure the orientations of grains in metals such as nickel, titanium and their alloys, with widespread use in high-value engineering [4].

Presently, there is a limited number of techniques for determining the crystallographic orientation of microstructure. Electron diffraction based techniques, such as electron back scatter diffraction (EBSD) are common. The spatial and angular resolution of these techniques is unparalleled [5]. However, there are significant limitations on the area of interrogation due to preparation/processing costs and the need for a vacuum chamber. Large scale orientation determination has often relied on etchant based approaches [6]. Whilst these can provide rapid measurements, orientation accuracy is often compromised [7]. Acoustic wave measurements provide a credible alternative, allowing large areas to be probed without compromising surface integrity at significantly increased acquisition rates.

The variations in material elasticity with crystalline orientation have previously been exploited to image the surface grain structure by acoustic surface wave (SAW) velocity measurements [8]. This work has been extended to recover the exact grain orientations in materials of cubic crystal structure [9,10]. In this paper, we extend this approach to hexagonal materials and describe the methodology in detail, exploring the limitations and accuracy of this methodology. The prevalence of titanium through safety critical sectors such as aerospace and healthcare, gives an industrial context to the need to understand the ability to map crystallographic texture in hexagonal materials. Furthermore, hexagonal crystal structures exhibit unique acoustic properties, making it particularly worthy of investigation.

Common engineering metals normally have one of five crystal

* Corresponding author.
E-mail address: wenqi.li@nottingham.ac.uk (W. Li).

https://doi.org/10.1016/j.ultras.2020.106171
Received 10 December 2019; Received in revised form 7 March 2020; Accepted 5 May 2020
Available online 29 May 2020

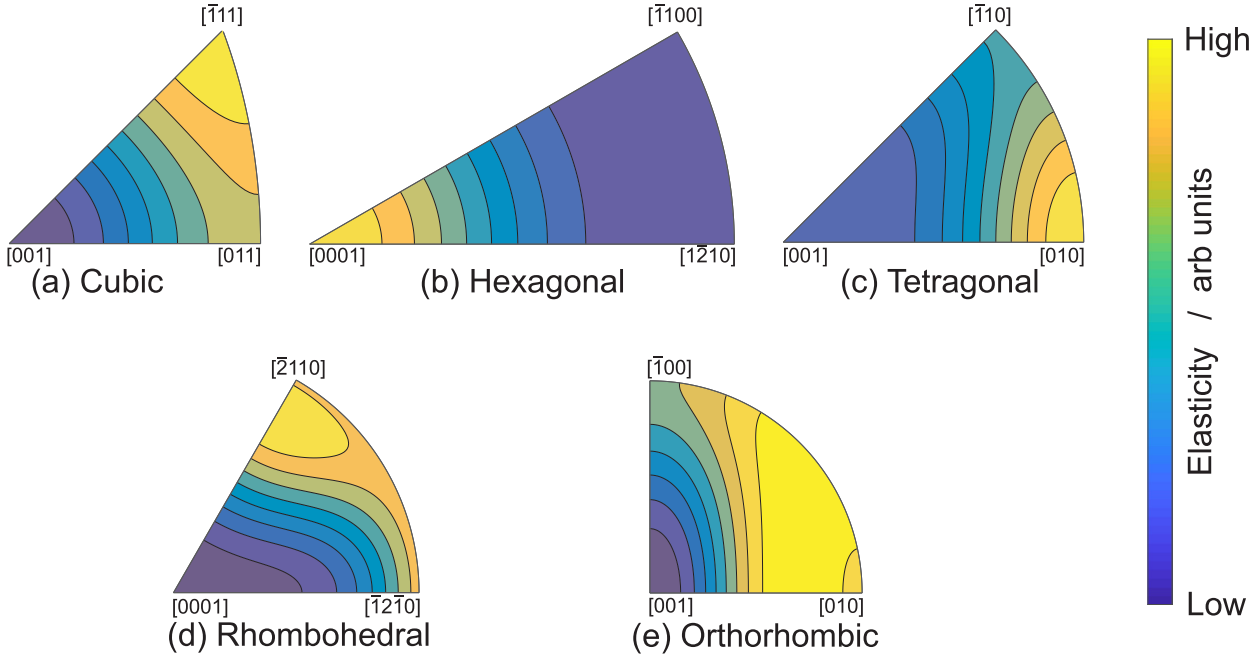

Fig. 1. Stereographic projections of directional Young's modulus for different crystal classes.

structures: cubic, hexagonal, tetragonal, rhombohedral and orthorhombic. The resulting shape of the elasticity tensor for an exemplary material of each crystal class is shown in Fig. 1. As can be seen in Fig. 1(b) hexagonal tensors exhibit mechanical transverse isotropy; rotations about the c-axis do not change the directional mechanical properties of the crystal. In contrast, all other crystal class systems, including the previously reported cubic, show two axes where the elasticity varies. Given the relationship between material elasticity and SAW wave velocity, first reported by Farnell [11], this phenomena will undoubtedly impact the ability to determine the orientation of hexagonal crystal structures.

Furthermore, in addition to the pure Rayleigh mode SAW, a supersonic wave mode is known to propagate on certain planes in hexagonal crystals, as defined by Ting and Barnett [12]. With these unique properties in mind, it is of interest to understand the ability of SAW measurements to map the orientation of hexagonal crystals.

The experimental results presented in this work are based on the acoustic microscopy technique spatially resolved acoustic spectroscopy (SRAS), but the approach and results used through are deliberately general so as to be applicable to any experimental technique which can capture SAW velocity measurements at varying propagation directions to build up acoustic velocity surfaces. Techniques used to capture such measurements include point source-receiver [13], scanning acoustic microscopy [14] and resonant ultrasound spectroscopy (RUS) [15]. RUS has been similarly been used to recover orientation in hexagonal crystals. This field of work relies upon exploiting the relationship between crystalline orientation, elasticity and SAW velocity in anisotropic materials. The work discussed thus far attempts to find the orientation in materials with known elasticity - as is the thrust of this work, however it is feasible to invert the problem and find the elastic constants of a material with known orientation. For example, Kim and Rokhlin have provided used line-focus microscopy, alongside through modelling of SAW behaviour, to calculate the elastic constants in several single crystal Ti-alloys [16].

The present paper extends previous work to show how linear acoustic surface wave measurements may be used to recover crystalline orientation in hexagonal materials, focussing on both theoretical limitations and current experimental reality. We intend this paper to serve as a guide to the accuracy and limitations for both those in the ultrasonics and materials communities considering the use of SAW measurements for orientation determination.

2. SAWs and crystallographic orientation

It has long been understood there exists a three way relationship between SAW velocity, material elasticity and crystalline orientation [17]. Elastic constants for single phase engineering materials are widely available in literature, allowing the velocity of SAWs to be calculated as a function of crystallographic orientation. Although it is complicated to solve for the SAW velocity at an arbitrary direction analytically [18], numerical solutions can be determined [11,19,20]. This approach with practical modifications has previous been reported [9]. Other alterations have been suggested to these numerical methods, in order to reduce computation time [21]. The database of numerical solutions of velocity surfaces was across for planes across the orientation space - this database was termed the forward model henceforth.

The number of calculations required depends primarily on the angular increment on each velocity surface and between the planes. A typical model, such as those used throughout this study have 1 degree intervals on the velocity surface and 1 degree between planes. For context, the calculation of such a model took less than 1 min. It is important to note,

It is customary to represent the orientation by three angles defining the rotation from the specimen axes. Euler-Bunge notation uses ZXZ rotations, as shown in Fig. 2a to represent the angles (ϕ_1, Φ, ϕ_2), and was used throughout this work. In reference to the forward model, Φ represents a unique velocity surface and ϕ_1 represents a rotation of this velocity surface.

2.1. SAW Properties of hexagonal crystals

Fig. 2b and c plot the acoustic velocity surfaces seen on the principal planes using three sets of elastic constants for hcp titanium, given in Table 1. The constants sets from the work of Fisher et al. and Hearmon gave similar results on both principal planes. The Ogi constants set was notably faster, primarily attributed to a change in the density. It should be noted these elastic constants vary significantly from those measured by Kim and Rokhlin for Ti-alloys [16]. The elastic constants sets for the

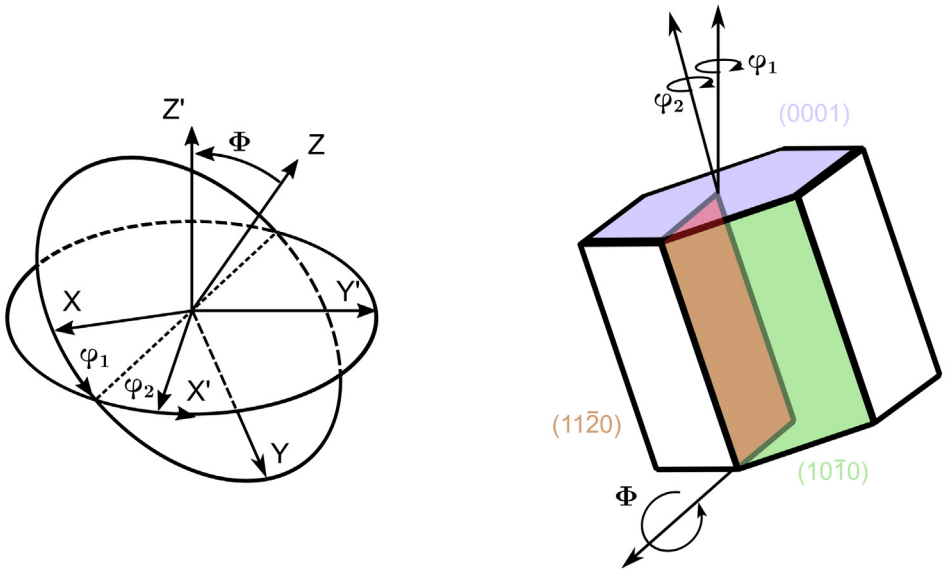

(a) Euler-Bunge angle definition.

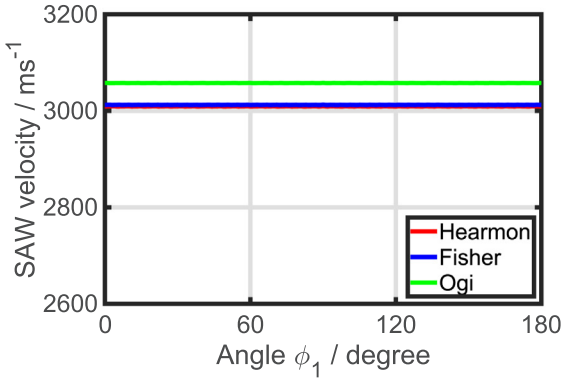

(b) {0001} plane SAW velocity.

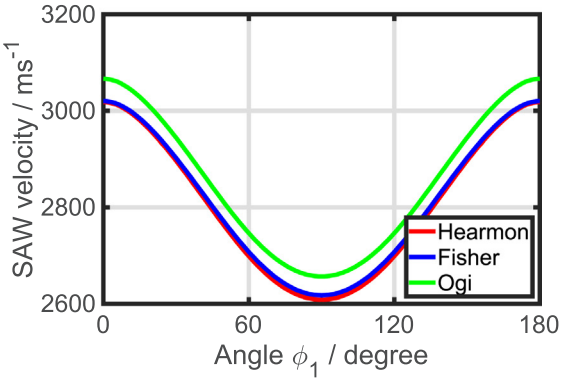

(c) {10$\bar{1}$0}/{11$\bar{2}$0} plane SAW velocity.

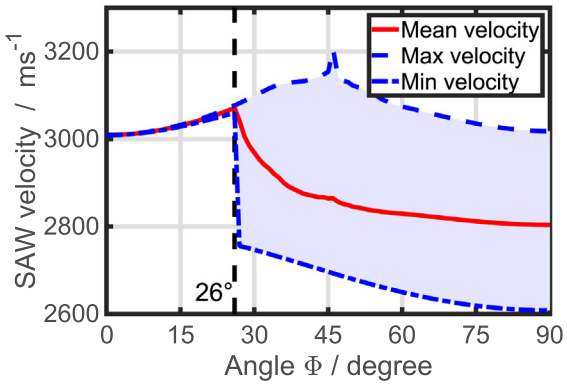

(d) Variation in SAW velocity across planes.

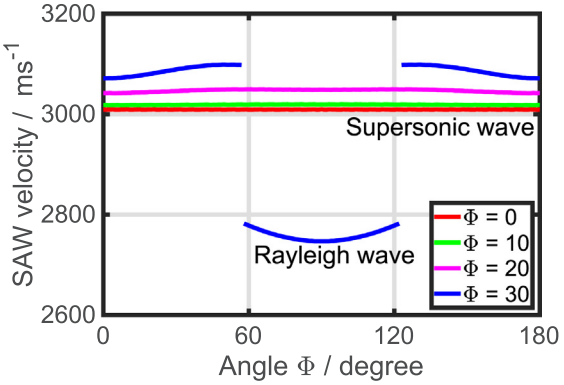

(e) Variation in SAW velocity across planes, showing mode hop from supersonic to Rayleigh wave, and isotropic nature near basal plane.

Fig. 2. SAW properties of titanium.

Ti-alloys produce velocity surfaces >200 ms^{-1} slower than those shown in Fig. 2. This demonstrate SAW velocity models for pure-Ti is not representative of Ti-based alloys, elastic constants must be specific to the material under evaluation.

As seen in Fig. 1, hexagonal tensors exhibit transverse isotropy. Consequently this leads to a few cases where elastic properties, and subsequently SAW velocity, do not vary with the crystal orientation. For example, the velocity surface seen on the basal plane {0 0 0 1} is isotropic - rotation of the velocity surface does not changed the SAW velocity - Fig. 2b. Fig. 2c, the characteristic acoustic velocity surface of the

Table 1
Elastic constants sets of titanium from literature.

Reference	c_{11} (GPa)	c_{12} (GPa)	c_{13} (GPa)	c_{33} (GPa)	c_{44} (GPa)	ρ (kg m^{-3})
Ogi et al. [22]	163.6	92.3	67.9	185.2	47.1	4429
Hearmon et al. [23]	160.0	90.0	66.0	181.0	46.5	4510
Fisher et al. [24]	162.4	92.0	69.0	180.7	46.7	4506

principal prism planes $\{1\ 0\ \bar{1}\ 0\}$ and $\{1\ 1\ \bar{2}\ 0\}$ are identical - the velocity surface is insensitive to changes in ϕ_2. This is to say, linear acoustic techniques cannot determine ϕ_2 by this method.

A final special case occurs when the Euler angle Φ of two planes are the same and both plane normals are in the same plane with axis Z, the Euler angle ϕ_1 of these planes can be narrowed down to either 0 °C or 180 °C.

Rayleigh SAWs are not found on the basal plane in titanium, instead the dominant surface wave mode on this specific crystallographic plane is a supersonic wave [21]. As the cut-plane tilts away from the basal plane ($\Phi \rightarrow 90$), this supersonic mode gives way to the subsonic Rayleigh SAW. This is shown in Fig. 2e, when $\Phi < 28°$ the dominant mode is a supersonic near-isotropic wave. At $\Phi = 28°$ a secondary slower mode can be seen to break off when $60° \leqslant \phi_1 \leqslant 120°$, this is the Rayleigh mode. Where two modes exist on a given plane, the transition is known as a mode hop. The forward model discriminated the dominant wave mode by calculating displacement of each mode.

2.2. Representing orientation data

Inverse pole figures (IPF) are the most common method of presenting crystallines orientation. Usually for EBSD captured datasets the IPF shows the combination of Euler angles Φ and ϕ_2, however an alternative representation is needed for angles Euler angles ϕ_1 and Φ as resolvable by linear acoustic techniques. Fig. 3, compares a traditional IPF (Euler angles Φ and ϕ_2) and the proposed c-axis map (Euler angles ϕ_1 and Φ). Both images have been generated from the same dataset as captured by EBSD. The c-axis map scales linearly for both ϕ_1 and Φ. Changes in hue represent variations in ϕ_1, similarly changes in saturation represent variations in Φ. The key in the c-axis map shows the orientation of the hexagonal crystal.

3. Orientation accuracy - simulation

The process of determining the orientation from the velocity is not straight forward. If two of the orientation, velocity or elastic constants are known then, in principle, the third can be computed. However, determining the orientation from the velocity and elastic constants is an ill conditioned problem that does not lend itself to an analytical solution [25]. The presence of experimental noise makes the direct inversion impractical and unreliable. Instead, the authors have proposed the process of cross-correlating the forward model (described in Section 2) with experimentally measured velocity surfaces [9]. This approach was more robust to experimental noise, and reducing the number of scanned directions. This method is known as the overlap function. The correct plane is that with the highest summed correlation value. Experimental work in the present paper was performed using spatially resolved acoustic spectroscopy (SRAS), but this approach to crystal orientation determination can be applied to all forms of multi-angle surface acoustic wave velocity measurement. Time-of-flight measurements will typically be in the time domain giving a 1D dataset; for SRAS, the results at a single direction are expressed as a Gaussian curve in the frequency domain. Thus, the inverse problem be solved with either 1D or 2D cross-correlation, to return the crystallographic orientation.

Essentially, the orientation of the hexagonal crystal is determined as the plane and rotation with greatest value in the figure of merit (FoM) space, the process to calculate the FoM is described as follows. The SRAS method uses a fixed grating and measures the frequency of generated ultrasound and in this case the experimental data from the SRAS measurement produces a plot of the signal amplitude vs frequency, for a fixed acoustic wavelength. Hence, the measurement provides a plot of signal vs velocity for each measurement direction on the plane $A(\theta, v)$, this is termed the velocity surface spectrum, where the plane is Φ, and ϕ_1 is the rotation angle on the plane. An example signal is plotted in Fig. 4a. An equivalent binary dataset, $v(\phi_1, \Phi)$, can be generated from the forward model database, one plane from this dataset is shown in Fig. 4b. These two datasets are then cross-correlated.

The FoM is the sum of $A(\theta, v(\phi_1, \Phi))$ for each plane and rotation, calculated according to Equation 1. An example figure of merit is shown in Fig. 4c. The location of the maxima across the FoM indicates the modelled database velocity surface which best matches the experimental dataset and hence the output crystallographic orientation for that measurement pixel.

$$F(\phi_1, \Phi) = \sum_{\theta=0}^{\theta=(n-1)/n\pi} A(\theta, v((\theta - \phi_1), \Phi)) \quad (n = 1, 2, 3...) \tag{1}$$

where n represents the number of evenly spaced velocity measurements used to determine the velocity. Apart from the special case of the basal plane, every velocity surface has a unique solution in the orientation space. Reducing the bandwidth of the signal A increases the correlation value of the correct solution relative to the noise from incorrect solutions.

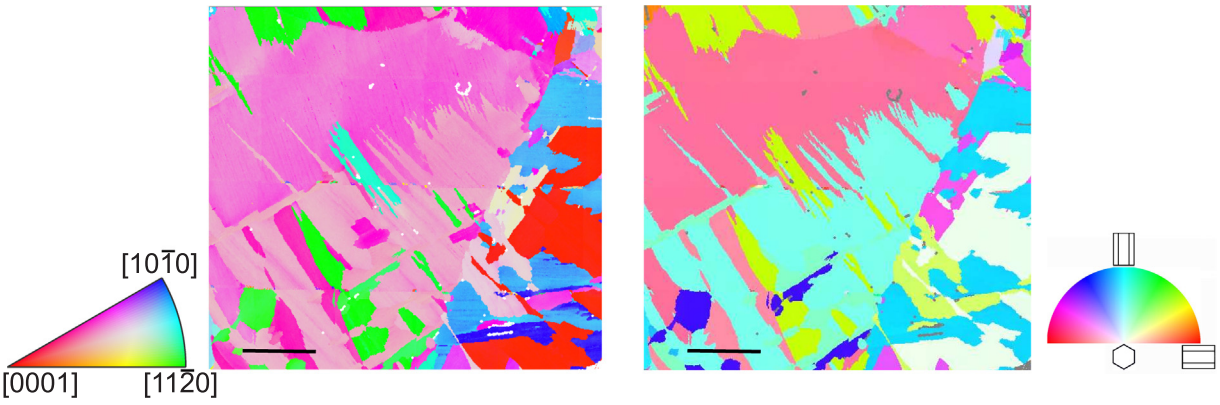

Fig. 3. Titanium orientation results by EBSD: IPF (left, Euler angles Φ and ϕ_2) and c-axis map (right, Euler angles ϕ_1 and Φ). These figures are plotted from the same dataset. The Φ orientation can be determined in both plots, for example the basal plane is seen as red in the IPF and white in the c-axis map. Scale bars indicate 500 μm.

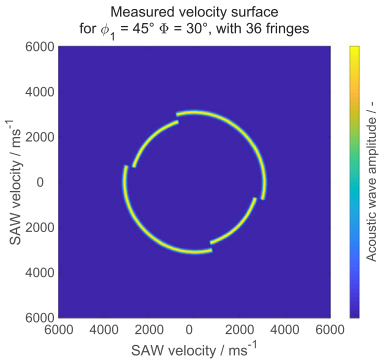

(a) Experimental velocity surface spectrum, this represents the measurement from one pixel in 360 directions with 36 acoustic fringes used for the measurement.

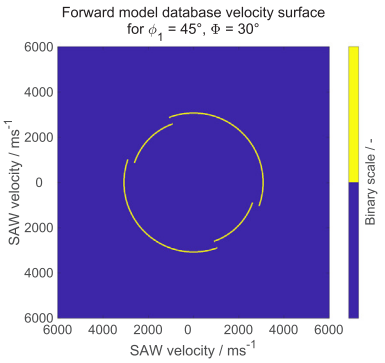

(b) Binary velocity surface from forward model database for Φ = 30°.

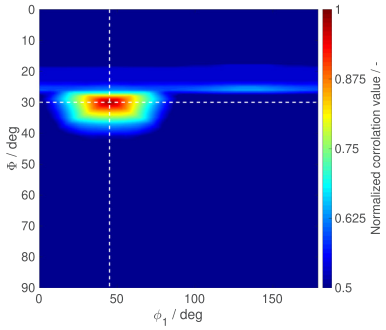

(c) Figure of merit from cross-correlation of (a) with forward model database, (b) is an example of one plane from this database. Dashed lines indicate correct orientation location. The intensity indicates the goodness of fit for that orientations database velocity surface, compared to the experiment.

Fig. 4. The inversion process for two sets of experimental data on the extreme ends of signal bandwidth. The measured velocity surface (a) is cross-correlated with the binary predicted velocities for each plane in the database, (b) is an example of the forward model for the plane Φ = 30°. Cross-correlation of the measured velocity surface with each entry in the forward model produces a figure of merit (c). The location of the maxima in the figure of merit indicates the calculated crystallographic orientation of the measured velocity surface, changing the signal bandwidth will affect the intensity of the unique solution compared to the background noise seen at incorrect orientations.

3.1. Simulation process

A simulation was devised to investigate the limitations and capability of SAWs to determine crystallographic orientation in hexagonal crystals. Table 2 explains the simulation procedure at a single pixel: an arbitrary plane and its calculated slowness surface is shown in (a). An experimental waveform was constructed based on the number of the fringes in the generation pattern and calculated velocity, with added experimental noise (b). The figures shown in the middle column are the fast Fourier transforms applied to the time domain waveforms at 0° and 135° respectively - transforming the signal to the frequency domain (c). Radial acoustic velocity surface in frequency domain and its fitted orientation result are shown in (d). This is generated for each plane between 0° ⩽ Φ ⩽ 90° at 1° intervals on the plane.

Table 2
Simulation procedure. An arbitrary plane (Φ = 45°) and its corresponding calculated slowness surface is shown in the left 2 figures. The waveforms at 0° and 135° direction of the slowness surface have been situated with different number of fringes and SNRs; the corresponding frequency response are in the middle column. The right figures show the orientation fitted result (in black dot) over the simulated data.

The plane & its slowness surface (a)	Waveform in time domain (b)	Frequency spectrum with noise (c)	Velocity spectrum with fitted results (d)
	8 fringes: FWHM = 550 ms^{-1}, SNR = 18 dB.		
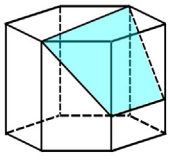	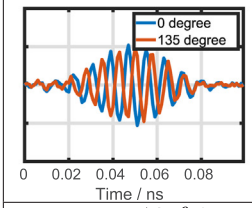	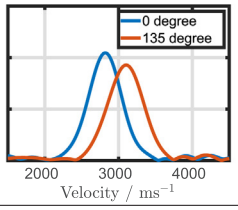	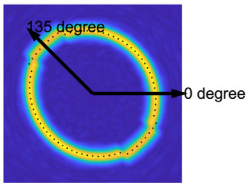
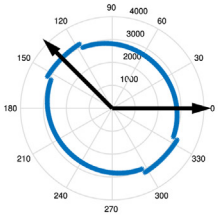	40 fringes: FWHM = 100 ms^{-1}, SNR = 0 dB.		
	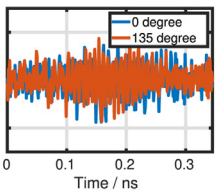	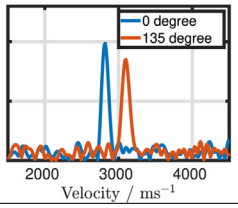	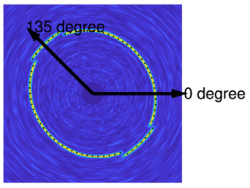

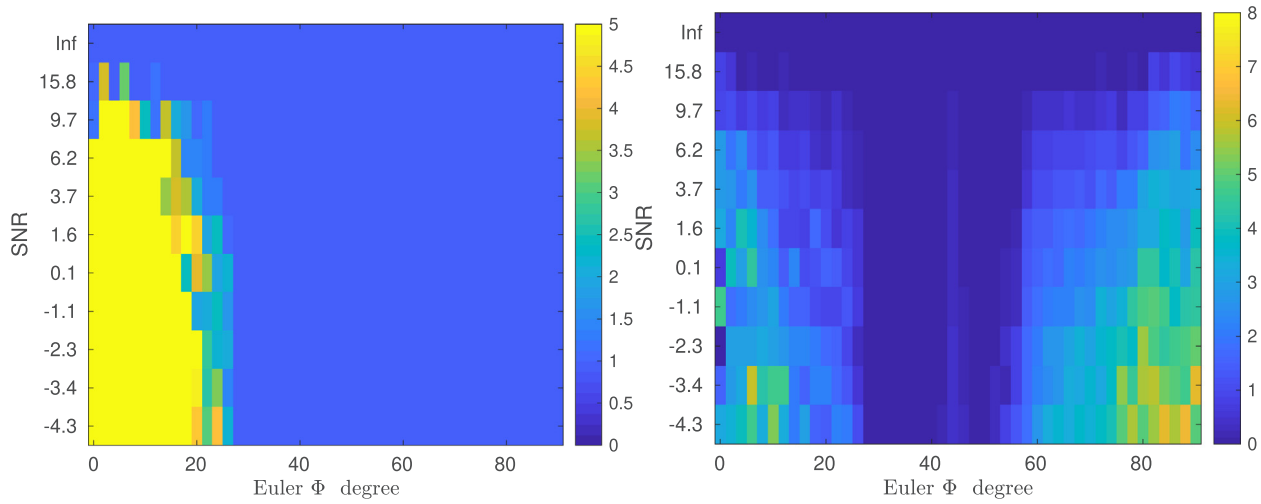

(a) Error of ϕ_1. (b) Error of Φ.

Fig. 5. Simulation results which show the error of angles ϕ_1 and Φ with respect to SNR and the crystallographic plane given by Φ. 30-fringe (150 ms^{-1} FWHM) generation pattern has been used in this simulation.

Throughout this work, the input signal bandwidth was defined by its full-width half maximum (FWHM), in the velocity domain and SNR in the time domain. However, it should be noted, the simulation was designed to mimic the current generation SRAS experimental, and thus the bandwidth was defined by the number of fringes in the generation patch, before being converted to ms^{-1} FWHM for plotting.

There are several experimental factors which may affect the accuracy of crystallographic determination: lattice anisotropy, velocity resolution, systematic measurement error, signal-to-noise ratio (SNR), number of measured SAW propagation directions and the interval between scan directions. The following sections will consider each of these in isolation to understand their impact on orientation accuracy.

3.2. Orientation dependent accuracy

It was firstly of interest to consider the fundamental limitations imposed by the acoustic properties of the hexagonal crystal. Fig. 5a, shows the orientation accuracy as a function of SNR and Φ angle - the accuracy of orientation recovery is dependant on the underlying orientation. When $\Phi \geqslant 28°$ the ϕ_1 error is <1°, for all simulated SNRs. When $\Phi \leqslant 28°$ the ϕ_1 error can increase to >5°, due to the isotropy of the velocity surface before the mode hop. Increasing the SNR of measurement was found to increase the range of Φ for which ϕ_1 can be determined. For example, at 0.1 dB large errors are seen $\Phi \leqslant 28°$, but this reduces to $\Phi \leqslant 18°$ for 9.7 dB.

Errors in Φ, Fig. 5b, were found to be lowest in the region of $28° < \Phi < 60°$. The $0° < \Phi \leqslant 28°$ results appear to match very well with the results from ϕ_1 error, suggesting the quasi-isotropy of the velocity surfaces (compared to the velocity sensitivity) in this region is again the cause of the determination errors. It was unclear at this stage why determination deteriorated for $60° < \Phi \leqslant 90°$.

In Fig. 5, the orientation determination accuracy is dependant upon the position within the orientation space. The uniqueness of the velocity surface is not consistent - highly unique surfaces increase the likelihood of the overlap function finding the true orientation. The velocity gradient, Fig. 6 is a good representation of this; where velocity gradients are large, velocity surfaces are more unique. Fig. 6a and b show the velocity gradients across ϕ_1 and Φ respectively.

Fig. 6b explains the improvement of determination in Φ in the region $28° \leqslant \Phi \leqslant 85°$, as seen in Fig. 5b. The presence of two SAW modes in this region, and thus a mode hop gives large velocity gradients (>10 ms^{-1}). Plotting the mean gradient shows the change in velocity between planes is small outside of this range, making the differentiation between neighbouring planes velocity surfaces increasingly difficult. The most extreme example of this is between $\Phi = 0°$ and $\Phi = 1°$, where there is only a 0.1 ms^{-1} change in velocity between the two planes. Similarly, Fig. 6a again highlights this isotropy before the mode hop. After this increasingly strong variations occur around $\phi_1 = 45°$ and $\phi_1 = 135°$. Fig. 6c is the product of Fig. 6a and b, giving an effective sensitivity map - regions with high velocity gradients are easier to determine. When sampling a velocity surface it is important to capture ϕ_1 angles with large velocity gradients.

It should now be clear that orientation accuracy is highly dependant on the anisotropy of the crystal. Hence, the data thus far applies only to hcp titanium and other hexagonal materials such as zinc will have a different characteristic accuracy response, which could be found through the methodology presented in this work. To show this, Fig. 7 plots the velocity variation across each plane for $0° \leqslant \Phi \leqslant 90°$. The variation was calculated by Eq. 2.

$$\Delta v(\Phi) = \frac{\max(v(\phi_1)) - \min(v(\phi_1))}{\frac{1}{N}\sum_{i=1}^{N} v(\phi_1)} \tag{2}$$

Fig. 7, the distinct mode hop in titanium can be seen at 28° and later around 45° in both Magnesium and Ruthenium. In Zinc however, no dominant supersonic mode is seen to propagate, instead the pure Rayleigh mode is seen across all planes. The large variations across the plane means orientation determination in zinc is relatively easier than titanium, and magnesium would be particularly difficult outside of the range $40° \leqslant \Phi \leqslant 50°$. Note, all materials show an isotropic basal plane as this is a shared property of all hexagonal crystals, imposed by the symmetry of the elasticity tensor. These curves inform on the velocity resolution that would be required experimentally to determine the crystalline orientation in each material.

3.3. Velocity resolution

If we consider next the most elementary experimental parameter, how well the SAW velocity can be measured. Two issues generally affect the velocity resolution in SAW measurements: (1) the measurement precision and (2) measurement correctness. Considering first the measurement precision, this can be equated to the signal bandwidth. Fig. 8a shows the relationship between angular error in determination of Φ and the FWHM, for six levels of noise. The result shows an exponential increase error with increasing FWHM. For all non-zero values of noise, there was error (>1°) when the FWHM is greater than 400 ms^{-1}. It can

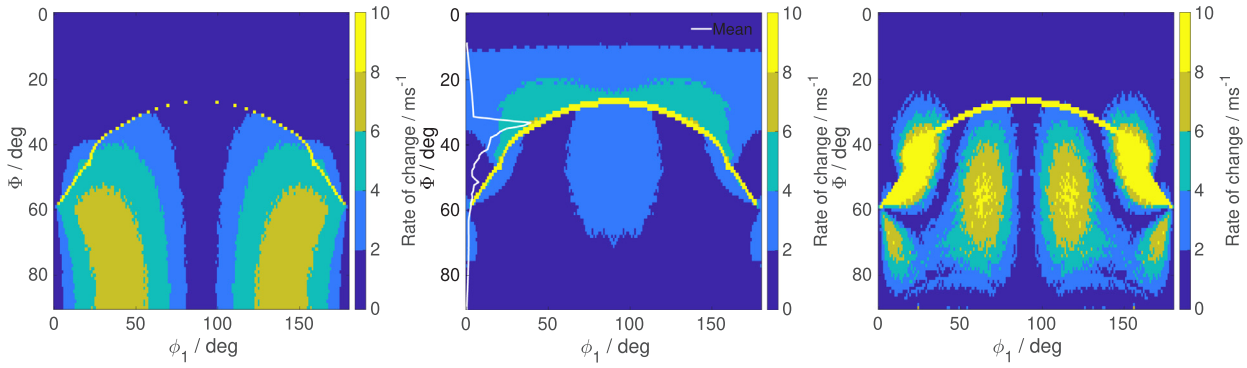

(a) Velocity gradient across ϕ_1.

(b) Velocity gradient across Φ.

(c) Combined velocity gradient effective sensitivity map.

Fig. 6. Velocity gradients across the orientation space. These are effectively sensitivity maps, showing the ease of determining the orientation by SAW measurement across the orientation space.

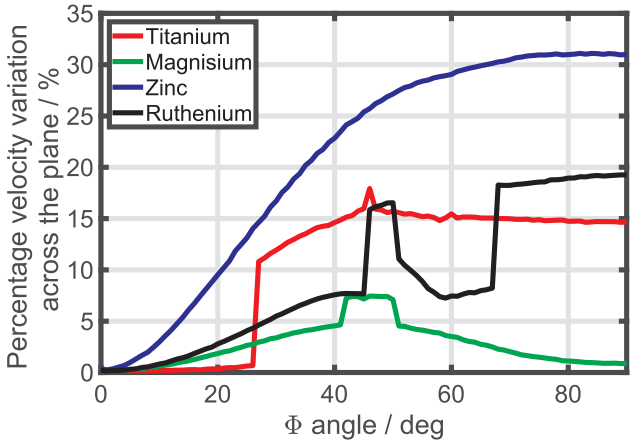

Fig. 7. Comparison of the SAW velocity variation across planes in four common hexagonal materials. As discussed, the distinct mode hop in titanium can be seen at around 28°. In Zinc however no dominant supersonic mode is seen to propagate, instead the pure Rayleigh mode is seen across all planes. Elastic constants for zinc, magnesium and ruthenium from [26–28].

be seen that reducing signal bandwidth below 20 ms^{-1} had a marginal impact on the determination accuracy and for most levels of noise 150 ms^{-1} is sufficient to match the resolution of the forward model. For non-zero levels of noise, errors converged with increasing FWHM. For FWHM greater than 1000 ms^{-1} all levels of SNR gave errors >2°, rapidly increasing to 10° by 2000 ms^{-1} FWHM. For context, typical SRAS experimental measurements have a velocity resolution of 400 to 800 ms^{-1}[29] as indicated in the figure, but can be controlled by changing the number of fringes in the generation patch and/or using temporal averaging.

Fig. 8b shows the impact of a systematic error in the velocity measurement. Velocity errors of ⩾ ±1% have a catastrophic effect on the angle determination, inducing errors of ⩾ 5° in Φ determination. Interestingly, the overlap function appears more tolerant to positive velocity errors. Signals of increasing bandwidth show a improved robustness to systematic velocity errors as expected, but as discussed in Fig. 8a, increasing bandwidth also reduces overall accuracy. This trade-off is a crucial consideration of an experimental system. In summary, the highest orientation accuracy can be achieved with very narrowband signals, however such measurements can be corrupted by even small systematic velocity errors.

3.4. Number of measured propagation directions and interval

The velocity surface of hexagonal crystals has both mirror and inversion symmetry, as discussed in the authors' previous paper [30]. According to the Nyquist theory, the minimum number of the measured direction is two, for hexagonal structure crystals. Fig. 9 shows the simulation results, also using 30 fringes (150 ms^{-1} FWHM) in the generation pattern: the angle Φ's accuracy varies to both the number of the directions scanned and the data SNR as expected, because the Φ is determined by the shape of the slowness surface.

The error of Euler angle ϕ_1 increased dramatically when only two directions were used, due to the inversion and reflection symmetry across all planes in hexagonal crystals. Hence at a certain rotation of the plane, velocities from two orthogonal directions are not enough to reliably identify Euler angle ϕ_1. In this case, the error may be close to 0 °C but is equally likely to be close to 180 °C. This poses the question, if only two-directions are scanned, which combination of the two directions is most efficient? The impact of varying the scan angle interval on the determination of ϕ_1 and Φ is illustrated in Fig. 10. It is seen that scan interval has little impact on the determination of the both ϕ_1 and Φ, so long as scans are not orthogonal.

4. Orientation accuracy - experimental

To validate the simulated models it is important to compare with experimental results. SRAS is a laser ultrasonic technique for crystallographic orientation determination, which non-destructively measures the SAW velocity on the material's surface. The concept of the SRAS technique has been presented by W. Li et al. [25,29]: a fringe pattern is imaged on to the specimen surface by placing an optical mask, with grating period λ, in the beam path of a pulsed laser. Thermoelastic absorption of the optical energy excites SAWs on the specimen surface, which propagate away from the generation patch with frequency, f. The surface perturbation due to SAW propagation can then be probed by a knife-edge detector. The combination of a broadband Nd:YAG laser and fixed fringe pattern is used, so that the local velocity v can be calculated, through $v = f\lambda$; the calculated velocity is a function of the mechanical response under the generation patch only. This makes SRAS robust to scattering and aberrations which plague time-of-flight measurements. Rotation of the grating pattern in the optical path allows control of the SAW propagation direction.

SRAS has previously been used to examine cubic crystal structure materials such as nickel-based alloys, aluminium and stainless steel; the SRAS orientation results have been compared to the EBSD technique [31]. More details on the instrumentation used in this experiment can

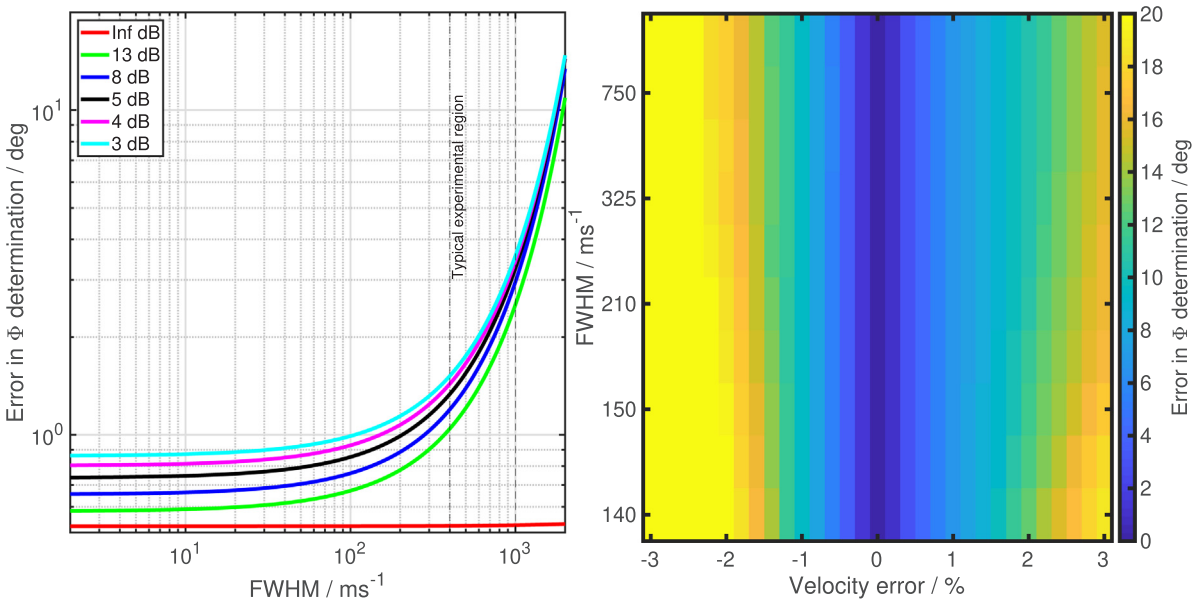

(a) Effect of varying signal bandwidth - representative to velocity measurement precision, on determination of Φ.

(b) Effect of a velocity measurement error on determination of Φ.

Fig. 8. Effect of systematic error in velocity measurement on the determination of Φ.

be found in Appendix A.

In this section, a series of SRAS datasets have been captured experimentally in a grade 1 commercially pure titanium (> 99% Ti) specimen of α-phase with hexagonal close packed structure. Specimens were ground and polished on the surface to be probed according to standard preparation for titanium [32], followed by a vibratory polish for 12 h in colloidal silica to prepare the samples for EBSD mapping, giving a final surface roughness of R_a < 100 nm - expressed by the arithmetic mean. Further information on the specific material studied, its preparation and EBSD scanning procedure can be found in [33].

Samples were first studied with EBSD, which has stringent requirements for surface finish, before been studied by SRAS. The current knife-edge type detector used in the SRAS experiment also requires a mirror-like finish but can be replaced by a detector which can unravel the speckle pattern from rough surfaces - two-wave interferometry, or are inherently insensitive - Fabry-Pérot interferometry [34]. The propagation of SAWs on rough surfaces can induce attenuation (due to conversion to bulk waves) and dispersion (due to diffraction of the SAW) [35], however the ability measure the SAW at an arbitrarily short distance from the generation patch minimises these effects in SRAS when dealing with optically rough specimens.

4.1. Full orientation map at standard scan parameters

The specimen was raster scanned to build up a velocity map, the process was then repeated a varying propagation directions so as to build-up a velocity surface for each point. Detailed scan parameters are given in Table 3. Based on these parameters, and using the models presented in Section 3, the predicted errors of this experimental study are expected to be $\phi_1 = 2.35°$ and $\Phi = 3.94°$.

It should be noted that the large scale EBSD map took 18 h to capture with multiple IPFs having to be stitched together, in comparison to 10 h it took to acquire all eighteen of the SRAS velocity maps. It would be possible to further reduce this by using a single velocity map to identify grains and capturing only single pixel velocity surfaces within these.

Fig. 11 compares the *c*-axis maps captured by EBSD and SRAS on a CP Ti specimen. In all datasets, non-measured points have been shown in grey. Due to the isotropy at and near the basal plane, grains which are close to the basal ($\Phi \sim 0°$, grains that appear white), angle ϕ_1 gave

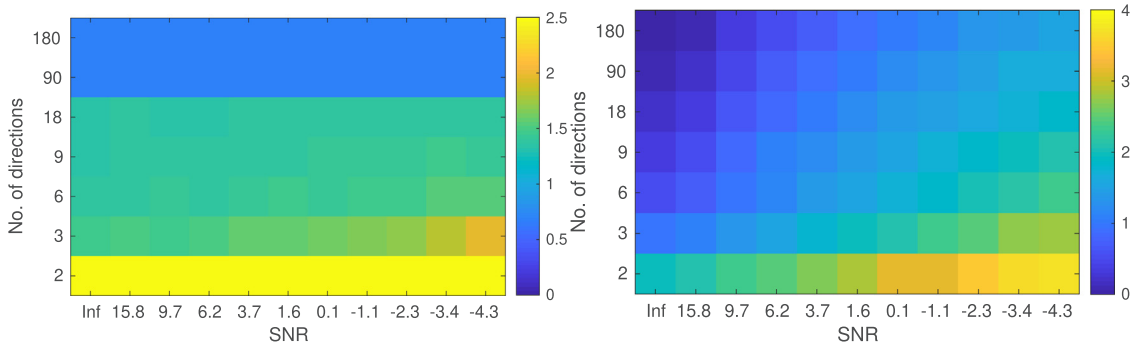

(a) Error of ϕ_1.

(b) Error of Φ.

Fig. 9. Simulation results which show the error of angles ϕ_1 and Φ with respect to SNR and the number of scanned direction. 30-fringe (150 ms^{-1} FWHM) generation pattern has been used in this simulation.

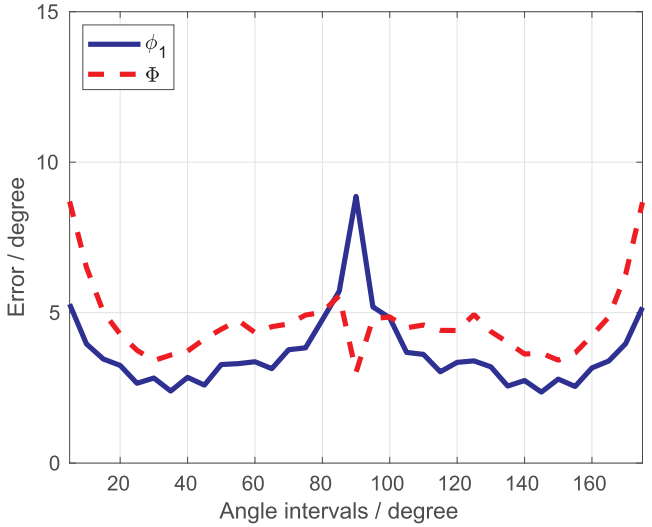

Fig. 10. Error bar of Euler angles against the intervals when using two directions. Simulation at 30 fringes (150 ms^{-1} FWHM).

Table 3
Experimental parameters for SRAS scan of CP titanium sample.

Scanned directions	18	Wavelength	24 μm
Scan direction spacing	10 °	Averages	1
Noise value	15 dB	Elasticity model	Hearmon
Signal bandwidth	480 ms^{-1}		
Expected Error ϕ_1	2.35°	Expected Error Φ	3.94°

inconsistent results. Beside this special situation, the other measurements are comparable. It is worth to noting that the spacial resolution of SRAS set in these experiments is 100 μm, which half of the generation patch diameter [29].

The expected errors based on the settings in Table 3 were smaller than those seen experimentally. Comparison of ϕ_1 between experimental measurements is difficult as this angle is taken in reference to the alignment of the sample. Slight misalignment of the specimen between experiments can cause errors of a few degrees. This is not the case for Φ.

There are three possible sources of dispcany between the experimental and simulated errors, these are discussed in the order of likelihood. Firstly, the simulated errors given Table 4 use a FWHM of 480 ms^{-1} to predict the accuracy of the orientation determination for each orientation in the specimen. This assumes that the FWHM is constant across the experiment, however this is not the case in reality. Changes in the optical properties (both reflectivity and laser generation efficiency will affect this) between grains and blemishes on the surface can cause local variations in the SNR, which would impact the final errors calculated.

Secondly, determination of the orientation by SAWs relies upon accurate knowledge of the elastic constants specific to the material under investigation. Given the variations seen between constants sets for Ti-α in Fig. 2a and b, using the Hearmon elastic constant set for the inversion - rather than those measured from the material - was the most probable source of disagreement between the simulated and experimental errors in this work.

Finally, the current SRAS instrumentation causes small deviations in the acoustic wavelength as the generation patch is rotated. In the system the divergent imaging beam passes through a tilted dichroic mirror; when the patch is rotated to a different direction for velocity measurements, the projection is slightly distorted by the mirror and causing the wavelength error. The wavelength was measured at each propagation direction and an average value used for the inversion process. The standard deviation of the acoustic wavelength in this experimental deployment was ~ 70 nm. If a 70 nm error in acoustic wavelength was true at every propagation direction this would be sufficient to cause an error of up to 2° in Φ determination (based on simulations from Section 3.4). Future adaptions to the inversion process should allow for the specific wavelength at each propagation direction to be used to minimise errors from this source.

It is also possible to quantitatively compare the individual Euler angles, Fig. 11b and c compare ϕ_1 and Φ respectively, plotting the absolute angular difference on a pixel-by-pixel basis. In the comparative maps grain boundaries have been ignored.

4.2. Single pixel orientation at optimal experimental settings

The experimental settings of the previous section are commonly used as they offer sufficient velocity resolution without compromising spatial resolution or significantly increasing the scan time. However, when these factors are not of importance it is feasible to capture more detailed velocity surfaces. In this section the bandwidth of the signal and the number of scanned directions were pushed to their practical maximum.

Experimental data was captured at two points in the specimen (CP titanium). Detailed scan parameters are given in Table 5. Based on these parameters, and using the models presented in Section 3, the predicted errors of this experimental study were expected to be <1°, on both grains - given the forward model has been calculated with 1 degree between planes this is the maximum orientation resolution. As expected, these errors were significantly smaller than those suggested in Section 4.1 thanks to the improved velocity resolution. Orientation determination is again compared to EBSD.

Fig. 12 shows the measured velocity surfaces from the two grains, with the fitted acoustic surfaces superimposed. In both grain A and B the resultant planes are within the imagined 1° of the EBSD measurements. The planes Φ = 0° and Φ = 90° have also been superimposed to demonstrate the velocity range seen over the orientation space, and illustrate why reducing signal bandwidth aids determination.

Fig. 12c and d show the FoM plots for grain A and B respectively. It can be seen that the correct solution is well localised in both grains, thanks to the narrowband acoustic signal, meaning only a few planes have a high correlation value. In both planes it is shown that determination of ϕ_1 is easier than Φ. Finally, it appears the orientation is easier to localise in grain B than grain A. This is inline with the sensitivity across the orientation space, shown in Fig. 6c.

4.3. Number of experimentally scanned directions and interval

Finally, the effect of number of scanned directions and the interval has been investigated experimentally (simulated results shown in Section 3.4.), for experimental parameters as given in Table 3. From Fig. 13a, the experimental results show good agreement with the simulated data sets, within 2° for both ϕ_1 and Φ, following the same trend, with errors increasing with fewer scanned directions.

Fig. 13a plots the simulated and experimentally determined errors when using two direction scans with varying interval, with experimental parameters as given in Table 3. Both the simulated and experimental data show little influence in the determination of either ϕ_1 and Φ, except from when scans are close to orthogonal. This is a useful result as 2 direction velocity vector maps have previously been used to illustrate approximate c-axis position from orthogonal scans [29]. In future, such maps should use a scan interval between [30°, 60°].

5. Conclusions

SRAS is part of a growing family of acoustic microscopy techniques which use SAW velocity measurements to quantitatively determine crystallographic orientation, however a thorough understanding of the

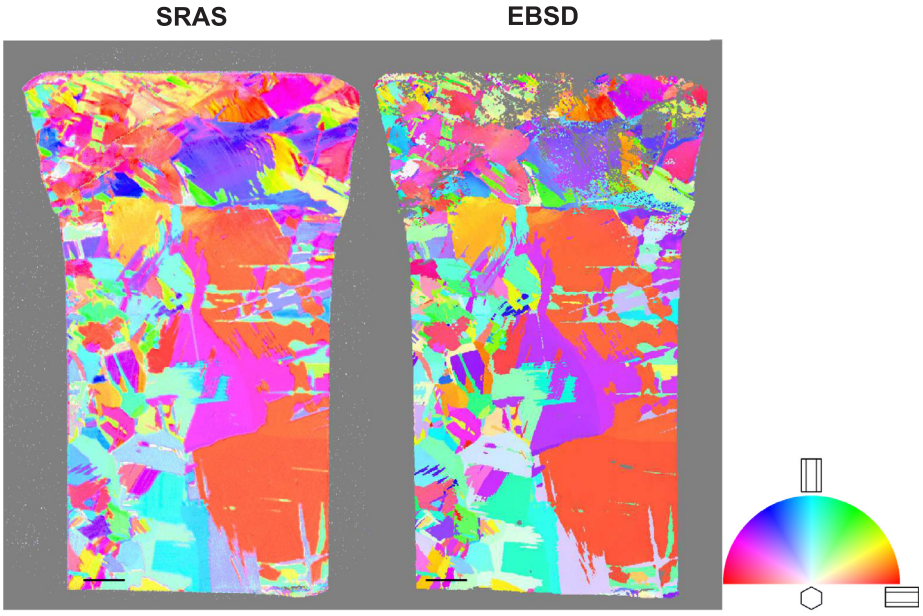

(a) Comparison of SRAS and EBSD c-axis maps, scale bars indicate 2 mm.

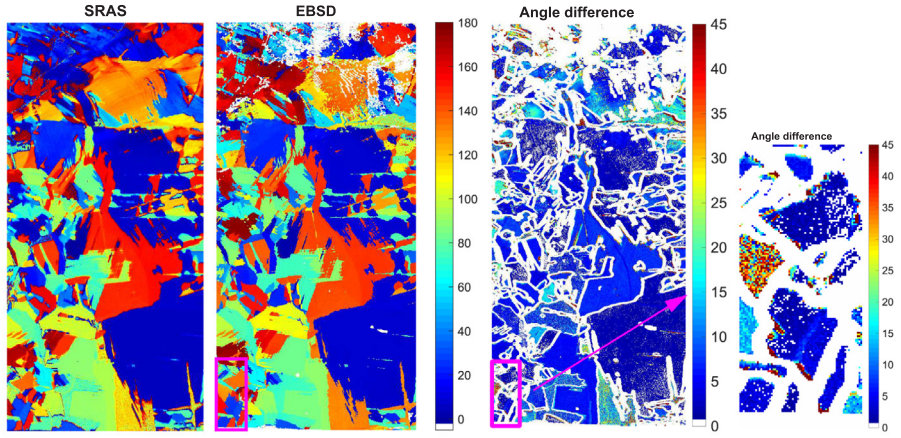

(b) Comparison of ϕ_1 angle.

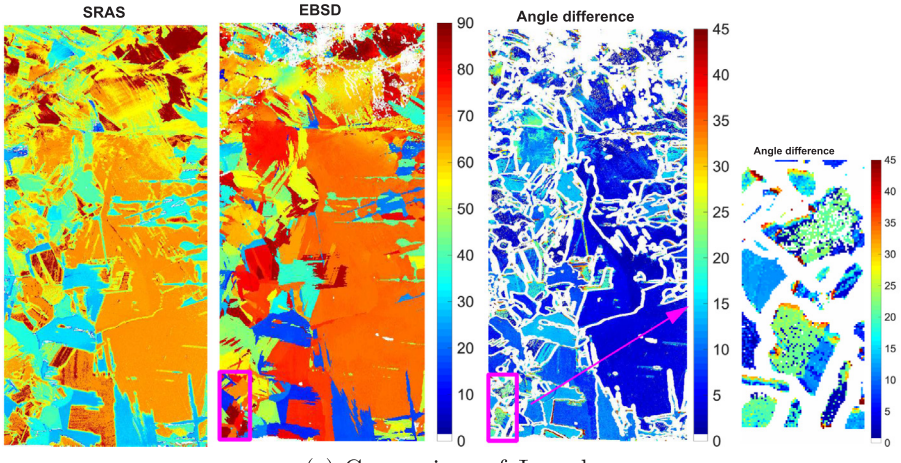

(c) Comparison of Φ angle.

Fig. 11. Comparison of c-axis orientation between (a) EBSD and (b) SRAS. Scale bar indicates 2 mm.

Table 4
Average error over the whole specimen: SRAS vs. EBSD.

	Simulated Error			Experimental Error		
Euler angles	Overall	$\Phi < 28°$	$\Phi \geqslant 28°$	Overall	$\Phi < 28°$	$\Phi \geqslant 28°$
ϕ_1	2.35 °C	2.71 °C	2.19 °C	5.14 °C	9.24 °C	4.81 °C
Φ	3.94 °C	10.43 °C	1.10 °C	6.99 °C	12.37 °C	6.48 °C

Table 5
High velocity resolution experimental parameters for SRAS scan of CP titanium sample.

Scanned directions	360	Wavelength	24 μm
Scan direction spacing	1 °	Averages	128
SNR value	19 dB	Velocity error	0 ms^{-1}
Signal bandwidth	190 ms^{-1}	Elasticity model	Hearmon
Expected Error			
Grain A $\Phi = 65°$	<1°	Grain B $\Phi = 40°$	<1°

accuracy and reliability of this orientation determination is not well understood and presents a key missing link in the uptake of acoustic techniques for this purpose. Cross-correlation has previously been used to find the best match between experimental velocity surfaces and predicted SAW velocities from a forward model database, allowing calculation of the crystallographic orientation. The present work has adapted this method for hexagonal crystals.

The main thrust of this work has been to investigate the sensitivity of orientation accuracy to experimental parameters when measuring SAW velocity. The calculated SAW velocity model of titanium has shown that its velocity surface is isotropic on the basal plane ($\Phi = 0°$), this prevents the determination of ϕ_2. As the cut plane tilts away from the basal plane, the velocity surfaces become elliptical, before the occurrence of a wave mode hop around 28°, where the dominant wave mode transitions from a supersonic wave to the normal Rayleigh wave. Accuracy in the determination of ϕ_1 was shown to vary across the orientation space, with errors of <2° degrees easily achievable in the Rayleigh wave range, for almost any level of SNR. Similar precision can be achieved in the supersonic zone (apart from the special case on the basal plane), but relies on higher SNR (>10 dB) or increased velocity

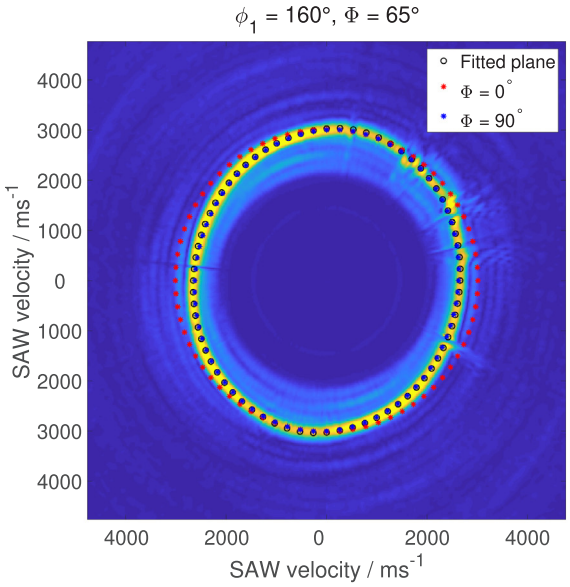

(a) Grain A velocity spectrum with with velocities from fitted plane superimposed.

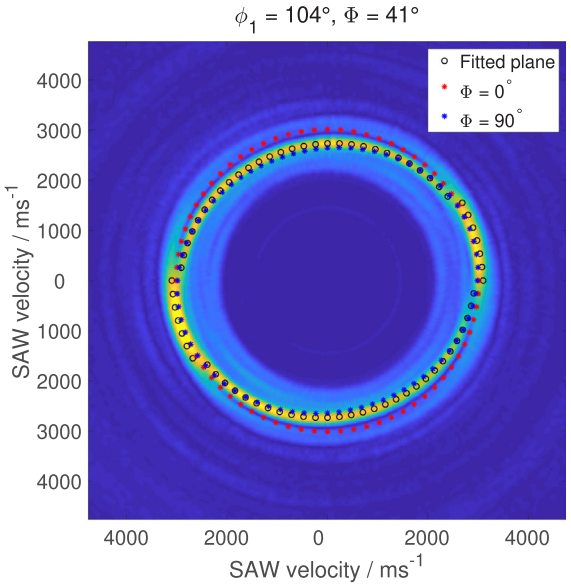

(b) Grain B velocity spectrum with velocities from fitted plane superimposed.

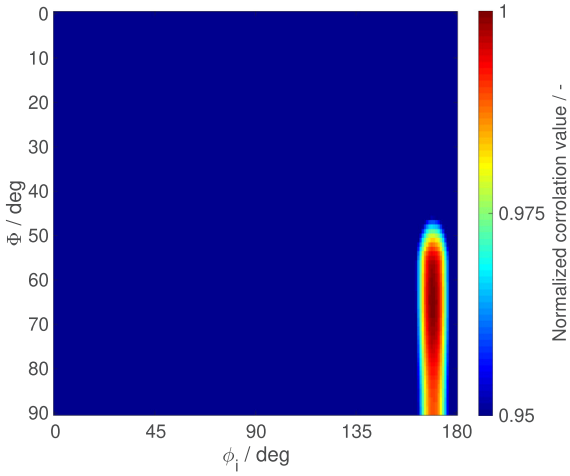

(c) Grain A FoM.

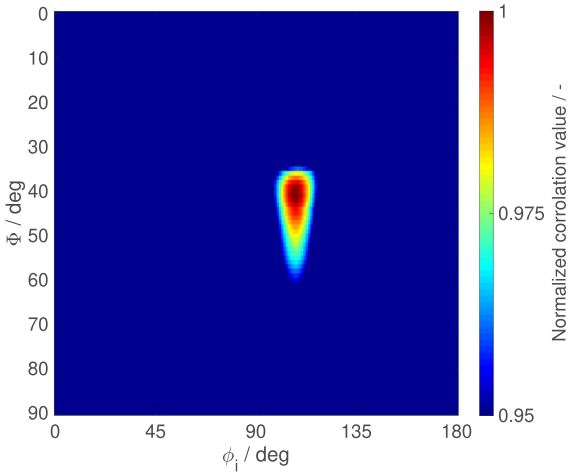

(d) Grain B FoM.

Fig. 12. Inversion of two high resolution velocity surface spectrum for two grains in CP titanium sample.

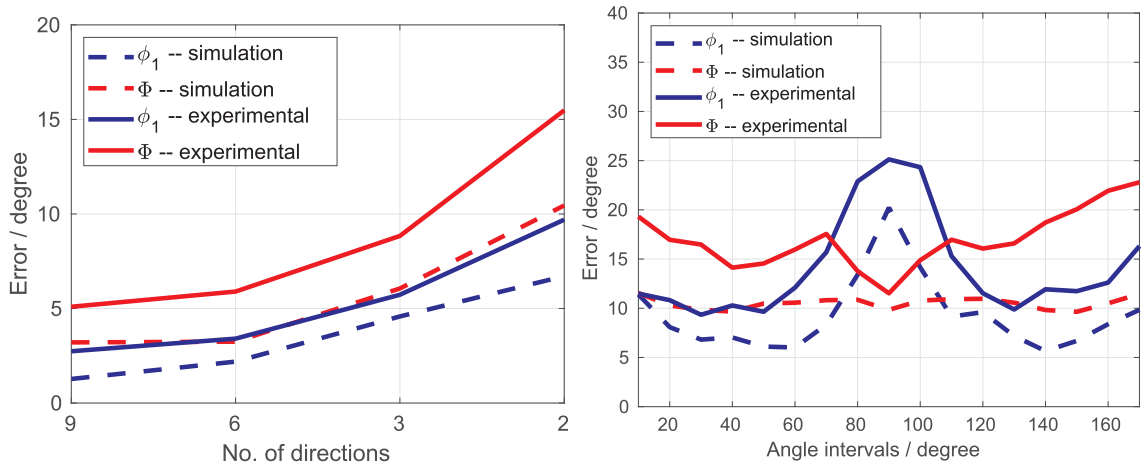

(a) Determination error of Euler angles against number of scanned directions.

(b) Determination error of Euler angles against scan interval, when using two directions.

Fig. 13. Experimental results, compared with simulation, for varying number of scanned directions and scan interval when using directions.

resolution. The orientation determination accuracy of Φ was shown to be primarily dependant on the accuracy of the SAW velocity measurement. A FWHM of >400 ms^{-1} is required to achieve average errors of 1° across the orientation space. Determination close to the basal plane becomes increasing difficult as velocity resolution must approach sub-ms^{-1} to differentiate between planes (e.g. $\Phi = 0°$ and $\Phi = 1°$). Conversely, determination in the region $40° \leqslant \Phi \leqslant 60°$ requires less precise velocity measurement as there is a greater change in velocity between planes in this region.

It was found for both ϕ_1 and Φ capturing >3 propagation directions significantly reduces the error in orientation determination, and is relatively insensitive to varying SNR levels. Increasing the number of directions to 90 reduces the associated error by a further ~ 0.5°.

To conclude this work two experimental studies have been compared to the simulation. Firstly a polycrystalline α-phase hcp titanium specimen has been scanned using SRAS using standard parameters (FWHM 480 ms^{-1} over 18 propagation directions) and the orientation output compared to measurements by EBSD. The orientation was found to compare well with EBSD with an average error of 4.81° and 6.48°, for ϕ_1 and Φ in the Rayleigh wave region, errors approximately double in the supersonic region ($\Phi < 28°$). Pertinently, the experimental errors are in good agreement with the expected errors from simulation (overall errors are 2.8° for ϕ_1 and 3.05° for Φ). Discrepancies are suggested to be from variation in the acoustic wavelength, inaccurate elastic constants and variation in the FWHM across the specimen. A second measurement with higher velocity resolution and increased scanning angles (FWHM of 190 ms^{-1} over 360 propagation directions) was made in two grains. With these scanning parameters orientation errors were expect to be reduced to less than 1 deg, which was found when comparing the calculated orientation to EBSD. The second experimental setting represents the highest resolution that is currently practically achievable.

Different hcp materials exhibit varying levels of anisotropy across the orientation space. To this end, given the material anisotropy is an important parameter in the determination of crystallographic orientation, the material specific analysis shown in this work is applicable to only pure α-phase titanium, however the method may be applied to any other hcp materials or elastic constant sets. Given the reliance on accurate knowledge of elastic constants for orientation determination, it would be a worthy development to integrate SAW measurements for orientation with a system for direct measurement of elasticity.

Declaration of Competing Interest

The authors declare that they have no known competing financial interests or personal relationships that could have appeared to influence the work reported in this paper.

Acknowledgements

This work was supported by the Engineering and Physical Sciences Research Council [Grant No. EP/S013385/1]. The authors are grateful to Prof. D. Rugg of Rolls-Royce plc for the provision of material. The authors would also like to thank the Royal Society for the travel grant IEC\R3\170081 which facilitated this study.

Appendix A. Instrumentation

The SRAS instrument used in this work is built around a broadband Q-switched laser for the thermoelastic generation of SAWs. This laser provides 1.6 ns pulses with pulse energies of 150 μJ at a repetition rate of 2 kHz. The short laser pulses allow a wide operating range for the generation of the acoustic waves from the low MHz to 100s of MHz. The breadth of this source allows the instrument to be flexible in terms of spatial and velocity resolution, control of the velocity resolution is particularly important for the work at hand. The optical arrangement of the system is shown in Fig. 14a. The Q-switched laser is used to illuminate an optical mask. The mask is a chromium pattern on a fused quartz substrate; this pattern is imaged to the sample surface. The line spacing and magnification of the imaging system determine the wavelength of the acoustic waves that will be generated. Throughout this work a 5:1 reduction has been used when imaging the generation patch on the sample surface, giving an acoustic wavelength of 24 μm. This is achieved by a long working distance objective lens (Mitutoyo M plan APO × 10, focal length 20 mm) and a tube lens with focal length of 100 mm. The optical mask has an aperture that can be varied between 0.3 and 3 mm, and so after being re-imaged to the sample surface the generation patch size is between 60 and 600 μm. The mask is mounted on a rotation stage allowing the orientation of the generation patch when imaged on to the sample to be rotated, this facilities the propagation of SAW in vary directions. Fig. 14b shows the projected fringe pattern, in the nominal 0, 45 and 90° positions.

The detection laser is a fibre coupled 532 nm continuous wave laser with an output power of 200 mW. The beam passes through a polarizing

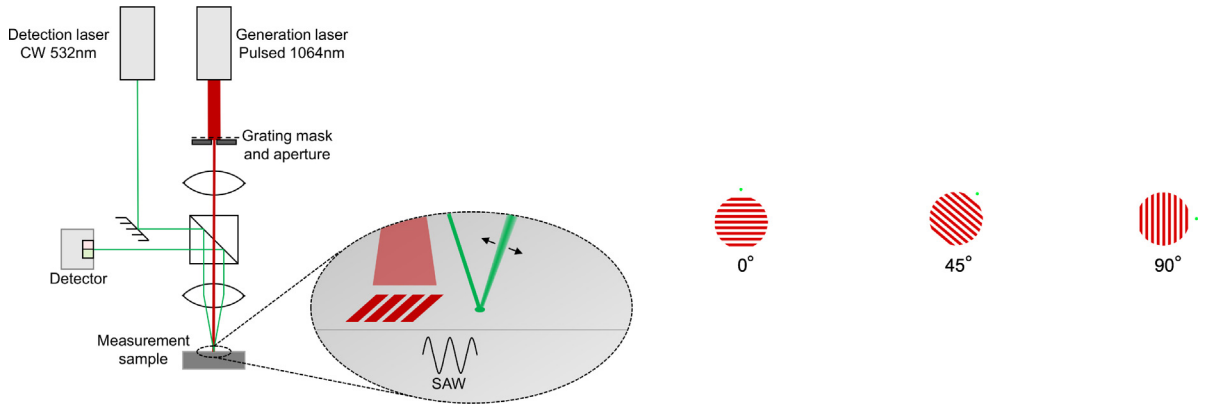

(a) Key components and layout of SRAS experiment. (b) SRAS generation patch at three rotations

Fig. 14. Diagram of basic SRAS system used in this work, showing primary components and the rotation of the generation patch to control the propagation direction of SAWs.

beam splitter (PBS) and quarter wave plate before being combined with the generation path by a dichroic mirror which reflects 532 nm light and transmits 1064 nm; it is then focused to the sample through the same imaging lens as the generation laser. The focal spot diameter is approximately 8 μm and positioned to the side of the generation region as shown in Fig. 14b. The position of the spot on the sample is controlled by a computer controllable piezoelectric steering mirror that allows the adjustment of the input angle of the detection beam to the objective lens. The returning beam from the sample surface retraces the same path back through the system, and passes through the quarter wave plate again; this causes the polarization to be flipped by 90° with respect to the input beam and the detection laser is now reflected by the PBS and is directed to the final lens of the system focusing the beam just beyond the split photodiode detector. The 8 μm probe beam spot size sets a limit to the minimum wavelength of the projected fringes; if the spot size is larger than half the acoustic wavelength, then the detection efficiency is significantly reduced and to work beyond this requires reducing the spot size by increasing the numerical aperture of the objective lens.

The SRAS system could use a number of different types of detectors, sensitive to surface displacement or optical beam deflection, depending on the range of expected frequencies and the surface finish of the sample. For samples with strong specular reflections, the detector used is a knife edge detector, based on the principle of optical beam deflection; this is sensitive to the out-of-plane surface motion in one propagation direction. As the acoustic waves pass under the probe beam spot, it causes the beam to be deflected and if this motion is across the split photodiode we measure the presence of the propagating waves. To get such strong specular reflections a mirror-like finish is required, however the detector can be replaced by one which can unravel the speckle pattern from rough surfaces - two-wave interferometry, or are inherently insensitive - Fabry-Pérot interferometry [34].

References

[1] G. Steinle-Neumann, L. Stixrude, R.E. Cohen, First-principles elastic constants for the hcp transition metals Fe Co, and Re at high pressure, Phys. Rev. B 60 (1999) 791, https://doi.org/10.1103/PhysRevB.60.791.

[2] T.P. Gabb, J. Gayda, R.V. Miner, Orientation and temperature dependence of some mechanical properties of the single-crystal nickel-base superalloy René N4: Part II. Low cycle fatigue behavior, Metall. Trans. A 17 (1986) 497–505, https://doi.org/10.1007/BF02643956.

[3] V. Sass, M. Feller-Kniepmeier, Orientation dependence of dislocation structures and deformation mechanisms in creep deformed CMSX-4 single crystals, Mater. Sci. Eng. A 245 (1998) 19–28, https://doi.org/10.1016/S0921-5093(97)00709-0.

[4] T.M. Pollock, S. Tin, Nickel-based superalloys for advanced turbine engines: chemistry, microstructure and properties, J. Propulsion Power 22 (2006) 361–374, https://doi.org/10.2514/1.18239.

[5] R.R. Keller, R.H. Geiss, Transmission ebsd from 10 nm domains in a scanning electron microscope, J. Microsc. 245 (2012) 245–251, https://doi.org/10.1111/j.1365-2818.2011.03566.x.

[6] P. Dunsmuir, The use of polarized light for the examination of etched metal crystals and their orientation, Br. J. Appl. Phys. 3 (1952) 264–267, https://doi.org/10.1088/0508-3443/3/8/305.

[7] A. Speidel, R. Su, J. Mitchell-Smith, P. Dryburgh, I. Bisterov, D. Pieris, W. Li, R. Patel, M. Clark, A.T. Clare, Crystallographic texture can be rapidly determined by electrochemical surface analytics, Acta Mater. 159 (2018) 89–101, https://doi.org/10.1016/j.actamat.2018.07.059.

[8] Y. Hong, S.D. Sharples, M. Clark, M.G. Somekh, Rapid measurement of surface acoustic wave velocity on single crystals using an all-optical adaptive scanning acoustic microscope, Appl. Phys. Lett. 83 (2003) 3260–3262, https://doi.org/10.1063/1.1621091.

[9] W. Li, S.D. Sharples, R.J. Smith, M. Clark, M.G. Somekh, Determination of crystallographic orientation of large grain metals with surface acoustic waves, J. Acoust. Soc. Am. 132 (2012) 738–745, https://doi.org/10.1121/1.4731226.

[10] R. Patel, W. Li, R.J. Smith, S.D. Sharples, M. Clark, Orientation imaging of macro-sized polysilicon grains on wafers using spatially resolved acoustic spectroscopy, Scripta Mater. 140 (2017) 67–70, https://doi.org/10.1016/j.scriptamat.2017.07.003.

[11] G.W. Farnell, Physical Acoustics – Principles and Methods vol. VI, Academic Press, New York and London, 1970, pp. 109–166.

[12] T. Ting, D. Barnett, Classifications of surface waves in anisotropic elastic materials, Wave Motion 26 (1997) 207–218, https://doi.org/10.1016/S0165-2125(97)00027-9.

[13] J. Chai, T. Wu, Determinations of anisotropic elastic constants using laser-generated surface waves, J. Acoust. Soc. Am. 95 (1994) 3232–3241, https://doi.org/10.1121/1.409987.

[14] S. Sathish, M. Mendik, J.H. Cantrell, W.T. Yost, Elastic constants and crystal orientation of individual grains of polycrystalline solids from scanning acoustic microscopy, J. Acoust. Soc. Am. 98 (1995) 2854–2857, https://doi.org/10.1121/1.413187.

[15] A. Migliori, J. Sarrao, W.M. Visscher, T. Bell, M. Lei, Z. Fisk, R. Leisure, Resonant ultrasound spectroscopic techniques for measurement of the elastic moduli of solids, Physica B 183 (1993) 1–24, https://doi.org/10.1016/0921-4526(93)90048-B.

[16] J.-Y. Kim, S.I. Rokhlin, Determination of elastic constants of generally anisotropic inclined lamellar structure using line-focus acoustic microscopy, J. Acoust. Soc. Am. 126 (2009) 2998–3007, https://doi.org/10.1121/1.3245032.

[17] T.C. Lim, Elastic Surface Wave Propagation in Anisotropic Crystals (Ph.D. thesis), Department of Electrical Engineering, McGill University, 1969 http://digitool.Library.McGill.CA:80/R/-?func=dbin-jump-full&object_id=128947&silo_library=GEN01.

[18] K. Tanuma, Stroh formalism and rayleigh waves, J. Elast. 89 (2007) 5–154, https://doi.org/10.1007/s10659-007-9117-1.

[19] M.Y. Dvoesherstov, V.I. Cherednik, A.P. Chirimanov, Calculation of surface acoustic waves in crystals using the global optimization procedure, Radiophys. Quantum Electron. 43 (2000) 719–729, https://doi.org/10.1023/A:1004886125954.

[20] P. Stoklasová, P. Sedlák, H.S.M. Landa, Forward and inverse problems for surface acoustic waves in anisotropic media: A Ritz-Rayleigh method based approach, Ultrasonics 56 (2015) 381–389, https://doi.org/10.1016/j.ultras.2014.09.004.

[21] M.R. Cherry, S. Sathish, R. Grandhi, A numerical method for predicting rayleigh surface wave velocity in anisotropic crystals, J. Comput. Phys. 351 (2017) 108–120, https://doi.org/10.1016/j.jcp.2017.09.002.

[22] H. Ogi, S. Kai, H.M. Ledbetter, R. Tarumi, M. Hirao, K. Takashima, Titanium's high-temperature elastic constants through the hcp-bcc phase transformation, Acta Mater. 52 (2004) 2075–2080, https://doi.org/10.1016/j.actamat.2004.01.002.

[23] R.F.S. Hearmon, The elastic constants of anisotropic materials — II, Adv. Phys. 5

(1956) 323–382, https://doi.org/10.1080/00018732.1956.tADP0323.
[24] E.S. Fisher, C.J. Renken, Single-Crystal Elastic Moduli and the hcp →bcc Transformation in Ti, Zr, and Hf, Phys. Rev. 135 (1964) A482–A494, https://doi.org/10.1103/PhysRev.135.A482.
[25] W. Li, Laser Ultrasonic Method for Determination of Crystallographic Orientation of Large Grain Metals by Spatially Resolved Acoustic Spectroscopy (SRAS) (Ph.D. thesis), University of Nottingham, Electrical and Electronic Engineering, 2012 https://ethos.bl.uk/OrderDetails.do?uin=uk.bl.ethos.559555.
[26] H.M. Ledbetter, Elastic properties of zinc: a compilation and a review, J. Phys. Chem. Ref. Data 6 (1977) 1181–1203, https://doi.org/10.1063/1.555564.
[27] L.J. Slutsky, C. Garland, Elastic constants of magnesium from 4.2 k to 300 k, Phys. Rev. 107 (1957) 972, https://doi.org/10.1103/PhysRev.107.972.
[28] B.D. Pandey, D. Singh, P. Yadawa, Ultrasonic study of osmium and ruthenium, Platin. Met. Rev. 53 (2009) 91–97, https://doi.org/10.1595/147106709x430927.
[29] R.J. Smith, W. Li, J. Coulson, M. Clark, S.D. Sharples, M.G. Somekh, Spatially resolved acoustic spectroscopy for rapid imaging of material microstructure and grain orientation, Meas. Sci. Technol. 25 (2014) 1–11, https://doi.org/10.1088/0957-0233/25/5/055902.
[30] W. Li, J. Coulson, R.J. Smith, S.J. Lainé, S.D. Sharples, Crystallographic orientation determination of hexagonal structure crystals by laser ultrasonic technique, J. Phys: Conf. Ser. 684 (2016) 012001, https://doi.org/10.1088/1742-6596/684/1/012001.
[31] W. Li, J. Coulson, J.W. Aveson, R.J. Smith, M. Clark, M.G. Somekh, S.D. Sharples, Orientation characterisation of aerospace materials by spatially resolved acoustic spectroscopy, J. Phys: Conf. Ser. 520 (2014) 1–4, https://doi.org/10.1088/1742-6596/520/1/012017.
[32] W.L. Finlay, J. Resketo, M.B. Vordahl, Optical metallography of titanium, Ind. Eng. Chem. 42 (1950) 218–222, https://doi.org/10.1021/ie50482a011.
[33] S.J. Lainé, K.M. Knowles, 11$\bar{2}$4 deformation twinning in commercial purity titanium at room temperature, Phil. Mag. 95 (2015) 2153–2166, https://doi.org/10.1080/14786435.2015.1051157.
[34] S.D. Sharpies, R.A. Light, S.O. Achamfuo-Yeboah, M. Clark, M.G. Somekh, The SKED: speckle knife edge detector, J. Phys: Conf. Ser. 520 (2014) 012004, https://doi.org/10.1088/1742-6596/520/1/012004.
[35] A. Ruiz, P.B. Nagy, Laser-ultrasonic surface wave dispersion measurements on surface-treated metals, Ultrasonics 42 (2004) 665–669, https://doi.org/10.1016/j.ultras.2004.01.045.